

Developing a Fundamental Diagram for Urban Air Mobility Traffic Flow Based on Physical Experiments

Hang Zhou¹, Yuhui Zhai², Shiyu Shen², Yanfeng Ouyang^{2*}, Xiaowei Shi³, and Xiaopeng Li^{1*}

¹Department of Civil and Environmental Engineering, University of Wisconsin-Madison, Madison, WI, 53706, USA

²Department of Civil and Environmental Engineering, University of Illinois Urbana-Champaign, Urbana, IL, 61801, USA

³Department of Civil and Environmental Engineering, University of Wisconsin-Milwaukee, Milwaukee, WI, 53211, USA

*Corresponding authors. Email: yfouyang@illinois.edu (Yanfeng Ouyang), xli2485@wisc.edu (Xiaopeng Li)

Urban Air Mobility (UAM) is an emerging application of unmanned aerial vehicles (UAVs) that promises to reduce travel time and alleviate congestion in urban transportation systems. As drone density increases, UAM operations are expected to experience congestion phenomena similar to those observed in ground traffic. However, the fundamental characteristics of UAM traffic flow, particularly under real-world operating conditions, remain poorly understood. This study proposes a general framework for constructing the fundamental diagram (FD) of UAM traffic by integrating theoretical analysis with physical experiments. To the best of our knowledge, this is the first study to derive a UAM FD using real-world physical test data. On the theoretical side, we design two drone control laws for collision avoidance and develop simulation-based traffic generation methods to produce diverse UAM traffic scenarios. Based on Edie's definition, traffic flow theory is then applied to construct the FD and characterize the macroscopic properties of UAM traffic. To account for real-world disturbances and modeling uncertainties, we further conduct physical experiments on a reduced-scale testbed using Bitcraze Crazyflie drones. Both simulation and physical test trajectory data are collected and organized into the UAMTra2Flow dataset, which is analyzed using the proposed framework. Preliminary results indicate that classical FD structures developed for ground transportation are also applicable to UAM systems. Similar to ground traffic, UAM traffic capacity is strongly influenced by the adopted control law and key parameters such as safety spacing. Notably, FD curves obtained from physical experiments exhibit measurable deviations from simulation-based results, highlighting the importance of experimental validation in UAM traffic flow studies. Finally, results from the reduced-scale testbed are scaled to realistic operating conditions to provide practical insights for the design and management of future UAM traffic systems. The dataset and code for this paper is publicly available at <https://github.com/CATS-Lab/UAM-FD>. (The source code will be released upon acceptance of this paper.)

Key words: Drone; Urban Air Mobility; Fundamental Diagram; Traffic Flow

1. Introduction

Recent advances in hardware, such as lightweight composite materials, high energy-density batteries, and precision navigation technologies, have significantly improved the performance and expanded the applications of unmanned aerial vehicles (UAVs) or drones across various fields (Otto et al. 2018, Frachtenberg 2019, Zhou et al. 2023). Among these applications, Urban Air

Mobility (UAM), which uses drones to transport passengers or cargo at low altitudes in urban areas, has attracted notable attention due to its benefit of reducing travel and delivery time (Cummings and Mahmassani 2021). Although real-world deployment of UAM systems is still in its early stages, the growing number of drones operating in urban environments is expected to lead to congestion phenomena similar to those observed in ground transportation networks. However, the characteristics of UAM network congestion, which are an essential foundation for designing effective traffic management strategies, still remain poorly understood. Without a thorough analysis of UAM traffic properties, the operational efficiency advantages of UAM could diminish, and in some cases, even introduce potential safety risks.

In traffic flow theory, **fundamental diagram** (FD) has been key to describing the fundamental relationship between basic traffic measures (e.g., density vs. flow) under certain driver behavior/operational rules in a roadway channel (e.g., Greenshields (1935), Greenberg (1959)) or in a network (e.g., Daganzo and Geroliminis (2008), Saberi et al. (2014), Ambühl et al. (2020)). They help understand surface road traffic evolution over time and space, and have been widely applied to various research problems and engineering applications (Qu et al. 2017, Brilon et al. 2023). In the literature, various functional forms for not only traditional human-driven vehicles but also advanced transportation technologies have been adopted, such as multi-regime linear, polynomial, and exponential (Wu 2002, Zheng and Geroliminis 2016, Shi and Li 2021, Amirgholy and Gao 2017, Zhong et al. 2018). Only a limited number of studies in recent years have attempted to construct FDs in higher-dimensional spatial settings. For example, several studies have focused on pedestrian traffic. Daamen et al. (2005) developed traffic flow theory for pedestrians in two-dimensional domains. Flötteröd and Lämmel (2015) derived a bidirectional FD from microscopic principles and defined direction-specific flow-density relationships with bounded dynamics. Hoogendoorn et al. (2018) proposed a macroscopic FD for pedestrian networks. For a comprehensive review of pedestrian FDs, readers are referred to Vanumu et al. (2017). More recently, Cummings and Mahmassani (2021), Cummings and Mahmassani (2023), and Cummings and Mahmassani (2024) measured the density and flow data of drones in unstructured and structured 3D domains. Battista and Ni (2017) considered the influence of different varieties of wind, such as tailwinds, headwinds, and winds of consistent strength for drone operations while studying the FD in UAM. Haddad et al. (2021) calibrated the FD for UAM using a different collision avoidance mechanism based on the model proposed by Xue and Do (2019). However, as far as we know, all existing UAM FD results are based on only theoretical analyses or simulation-based approaches, and they have not yet been validated with physical tests. Consequently, many practical factors are excluded from consideration, such as the uncertainties inherent in practical scenarios, the mechanics and dynamics of drones, and the effects of individual drone control algorithms.

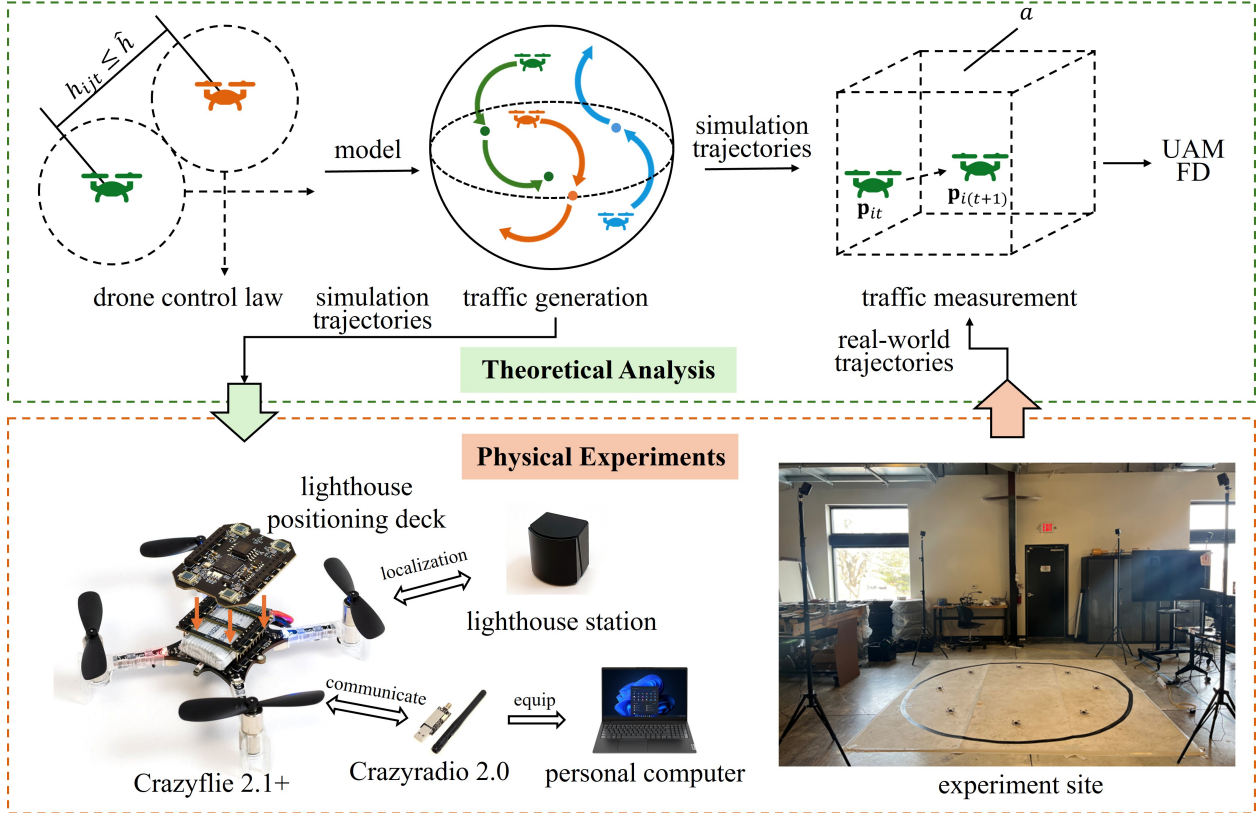


Figure 1 Overview of the proposed UAM traffic flow analysis method.

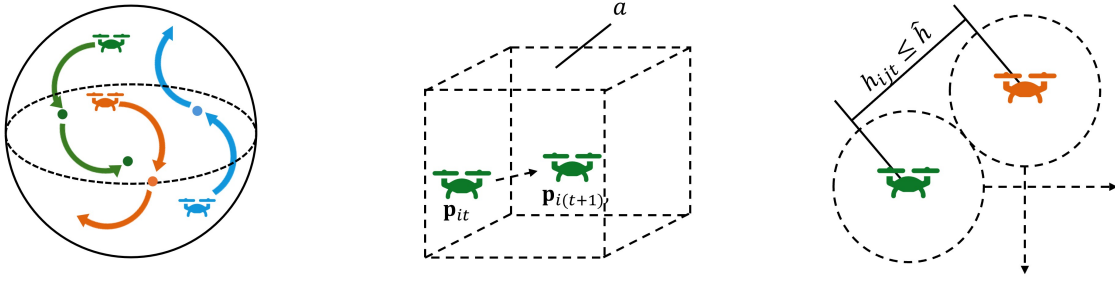
To effectively support informed decision-making in UAM traffic, it is crucial to develop an FD based on real-world drone traffic data. This paper proposes a general framework for constructing the FD for UAM, incorporating theoretical analysis and physical tests. Figure 1 illustrates the overall framework of the proposed method. On the theoretical side, we first design two control laws inspired by unsignalized intersection control, namely stop sign control and roundabout control. These control laws focus on collision avoidance algorithms when conflicts arise in the predicted future trajectories of drones, which is the main factors leading to congestion in UAM operations. Based on these control laws, we further develop simulation-based traffic generation methods to create diverse traffic scenarios and improve the generalizability of our findings. Finally, using traffic flow theory, we identify key measurements such as density and flow, and calibrate the FD of UAM traffic, which captures the macroscopic relationships and supports the analysis of UAM traffic properties. On the experimental side, to incorporate real-world disturbances such as drone dynamics and system delays, we conduct physical tests using a reduced-scale platform equipped with Bitcraze Crazyflie drones. Trajectories generated from simulation are used as reference inputs and transmitted as control commands to the drone swarm. The drones' actual movements are then recorded by the positioning system, and the collected trajectory data are analyzed

using FD theory to validate and refine the theoretical and simulation-based results. Preliminary calibration results indicate that the traditional FD structure remains applicable for describing the traffic flow characteristics of UAM. Moreover, some conclusions commonly observed in ground transportation are also applicable to UAM, such as the impact of different control laws and parameter settings on variations in the FD curve, and the significant enhancement of traffic capacity with smaller safety spacing settings. Besides, it was observed that the FD curves derived from physical tests tend to shift rightward compared to those obtained from simulations, which highlights the need for physical tests to corroborate and improve findings from pure theoretical or simulation studies. Finally, to obtain further insights into real-world UAM operations, we scale the results from the reduced-scale platform to realistic operating conditions, which can serve as a benchmark reference for future studies and applications.

To the best of our knowledge, this study is the first to construct a fundamental diagram (FD) for UAM traffic based on physical test data. Our work contributes to the literature in the following aspects:

- This paper proposes a **general framework for constructing the FD of UAM traffic**. The theoretical framework integrates the design of two drone control laws, a simulation-based UAM traffic generation method, and tailored traffic flow measurement and FD calibration methods for UAM systems. The proposed framework is modular and can be easily adapted to different UAM application scenarios.
- A reduced-scale UAM testbed is developed, and a **real-world UAM trajectory traffic flow dataset, UAMTra2Flow**, is collected to support UAM traffic flow studies. As the first publicly available dataset for UAM traffic, it encourages the research community to consider the impact of real-world disturbances and helps generalize existing findings to more practical operating conditions.
- Using the proposed framework and dataset, we **construct UAM traffic FDs based on physical test data**. Comparative experiments are conducted to analyze the factors that influence the FD, including the differences between simulation-based and physical-test-based FDs. In addition, results from the reduced-scale testbed are scaled to realistic operating conditions to provide benchmark reference data.

The remainder of the paper is as follows. Section 2 presents the theoretical analysis method for traffic generation, traffic measurement, and drone control law design. Section 3 describes the physical tests' details and shows the datasets collected by this study. Section 4 discussed the experimental results. Section 5 concludes this paper and suggests future research directions.



(a) Step 1: Traffic generation (b) Step 2: Traffic measurement (b) Step 2: Drone control law

Figure 2 Three steps of the theoretical framework.

2. Theoretical framework

This section presents a theoretical framework for UAM traffic flow data collection based on simulation, as well as the construction of a FD for UAM traffic. To introduce the key concepts and notations clearly, we follow the structure shown in Figure 2, which outlines three main steps: traffic generation, traffic measurement, and drone control law design. In Step 1, we define the experimental setup and generate drone trajectories under diverse traffic scenarios to cover a broad range of traffic states. Step 2 establishes an analytical framework for studying UAM traffic flow. It identifies the critical variables to be collected from experiments and guides the selection and calibration of an appropriate FD. In Step 3, we discuss the control strategies for individual drones, with an emphasis on collision avoidance algorithms when multiple drones' trajectories have conflict points. The trajectory scenarios generated through these steps are then used as input for drone control law in the physical tests, as detailed in Section 3. It is important to note that this study demonstrates a benchmark implementation of the three-step framework. Future work may explore extended variations within each step to design and conduct more comprehensive experiments.

2.1. General traffic information and traffic generation

This study considers UAM operations in a 3D unstructured airspace. Considering a given set of I drones, denoted as $\mathcal{I} = \{1, 2, \dots, I\}$, each drone performs a continuous sequence of flights that simulate real-world tasks, including package delivery, infrastructure inspection, and passenger transport. Each flight has a defined origin and destination (OD). To simplify the analysis and remove spatial boundary, drone movement is modeled on the surface of a spherical 3D space, denoted as \mathcal{A} . As shown in Figure 1(a), we assume that all OD points are located on the sphere with a uniform horizontal altitude. The reason for this assumption is that, in both the literature and real-world applications, urban airspace is commonly divided into multiple identical layers, and drones typically operate within a single layer. For example, recent airspace management

reforms in China propose dividing urban low-altitude airspace into layers with 15-meter vertical intervals, allowing drones to operate within separate horizontal planes (CCTV 2024). A similar urban airspace structure based on vertical layers is also discussed in Haddad et al. (2021).

In this UAM system, each drone starts from one origin and visits multiple consecutive destinations. During the flying, all drones keep the same desired cruising speed \bar{v} . The trajectory for each drone can be represented as a series of consecutive position data points in consecutive time steps $\mathcal{T} = \{0, 1, \dots, T\}$ with equal interval Δt , where T is the total number of time steps. As shown in Figure 1(b), the position vector for drone $i \in \mathcal{I}$ at time $t \in \mathcal{T}$ is denoted as $\mathbf{p}_{it} \in \mathbb{R}^3$. Denote the OD pairs for drone i as $(\mathbf{p}_{in}^O, \mathbf{p}_{in}^D)$, where $n \in \mathcal{N} := \{1, \dots, N\}$ indexes the sequence of flights and N is the total number of flights. Consecutive flights are connected, so that the destination of flight n coincides with the origin of flight $n + 1$, i.e., $\mathbf{p}_{in}^D = \mathbf{p}_{i(n+1)}^O$ for all $n \in \{1, \dots, N - 1\}$. The flight trajectory between any OD pair is assumed to follow the great-circle path on the spherical airspace. Given an origin point \mathbf{p}_{in}^O and a destination point \mathbf{p}_{in}^D , we generate intermediate positions along the unique great-circle arc connecting them using spherical linear interpolation (slerp) (Wikipedia 2025a). The slerp operator returns the point corresponding to a normalized arc-length parameter $\ell \in [0, 1]$ between two locations on the sphere. Therefore, we first compute the great-circle distance L between \mathbf{p}_{in}^O and \mathbf{p}_{in}^D using the spherical law of cosines (Wikipedia 2025b). Since the drone advances a physical distance of $\bar{v} \Delta t$ at each simulation step, the interpolation parameters then follow $\ell_h = h \bar{v} \Delta t / L$, $h \in \mathcal{H} := \{0, \dots, H\}$, where $H = \lceil L / (\bar{v} \Delta t) \rceil$. Applying slerp to each ℓ_i yields a time-consistent sequence of waypoints that discretizes the great-circle trajectory.

To represent a wide range of UAM traffic conditions, we consider different demand distributions, representing the geographic spread of customers' ODs. Three demand distribution scenarios are included: (1) randomly generated OD pairs continuously distributed on the spherical surface, mimicking online delivery with distributed customers; (2) origins and destinations are separated in different zones, respectively, mimicking segregated demand and destination patterns such as daily commute between residential and workplace areas; and (3) Random OD pair selection among fixed stations, where the eight stations are placed at the vertices of a cube inscribed in the spherical airspace, mimicking station-based delivery or station-to-station travel services.

2.2. Measuring UAM traffic

This section introduces the method used to measure UAM traffic flow.

2.2.1. Characteristics definition. Traditionally, the fundamental characteristics of ground vehicle traffic flow include density, flow rate, and speed. In 1D space, these metrics can be directly measured using Edie's generalized definitions (Edie 1963), based on trajectory data. However,

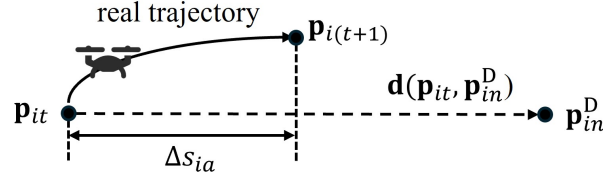


Figure 3 Illustration of the effective distance.

when the spatial dimension increases to 2D or 3D, the measurement approach requires modification. Prior studies, such as [Saberi and Mahmassani \(2014\)](#) and [Cummings and Mahmassani \(2021\)](#), have proposed extensions of Edie’s definitions to higher-dimensional traffic systems. This study adopts their approach.

Specifically, we consider a predefined two-dimensional measurement region $a \subset \mathcal{A}$ and a total time window \mathcal{T} . The volume of this time-space region is calculated as $|a| \Delta t T$, where $|a|$ is the area of region a , Δt is the sampling interval, and T is the number of time steps. For each drone i that enters region a during \mathcal{T} , its travel distance and time spent within the region are denoted as s_{ia} and t_{ia} , respectively. Then, the density and flow of drones in a , denoted by k_a and q_a respectively, can be calculated as:

$$k_a = \frac{\sum_{i \in \mathcal{I}} t_{ia}}{|a| \Delta t T} \quad (1)$$

$$q_a = \frac{\sum_{i \in \mathcal{I}} s_{ia}}{|a| \Delta t T}. \quad (2)$$

However, unlike the traditional car-following behavior observed on 1D highways, drones in this scenario may not only change their speed but also deviate from their planned paths to avoid potential collisions with other drones approaching from various directions. These potential detours must be considered in the analysis. Therefore, the measured distance s_{ia} represents the effective distance, i.e., the distance traveled by drone i projected onto the direction toward its next destination. Figure 3 illustrates this definition. The dashed line indicates the nominal direction from the current position \mathbf{p}_{it} to the destination \mathbf{p}_{in}^D , while the solid line shows the actual trajectory from \mathbf{p}_{it} to $\mathbf{p}_{i(t+1)}$. Only the projection of the actual trajectory onto the nominal direction contributes to the effective distance s_{ia} . Define the unit tangential direction from position \mathbf{p}_1 to \mathbf{p}_2 as $\mathbf{d}(\mathbf{p}_1, \mathbf{p}_2)$, which can be obtained using the slerp operator introduced in Section 2.1. Accordingly, the effective distance increment at time t is computed as

$$\Delta s_{it} = (\mathbf{p}_{i(t+1)} - \mathbf{p}_{it}) \cdot \mathbf{d}(\mathbf{p}_{it}, \mathbf{p}_{in}^D). \quad (3)$$

2.2.2. Region partition. To obtain meaningful macroscopic traffic measurements, it is essential that each measurement region a contains traffic conditions that are approximately homogeneous. If the entire spherical airspace \mathcal{A} were treated as a single measurement region, the resulting

flow and density would mix fundamentally different traffic states, i.e., drones flying at free-flow speeds and drones engaged in congestion under high-density conditions would be aggregated together. As a consequence, the resulting flow–density pairs do not correspond to a point on the FD but instead represent a linear combination of multiple points on the FD.

To avoid this issue, we apply a region partition technique is to compute flow–density pairs not from a single global region but from a set of smaller and homogeneous subregions, which reduces the likelihood that fundamentally different traffic states are aggregated within the same measurement region. Specifically, the spherical airspace \mathcal{A} is partitioned into M non-overlapping regions $a_1, a_2, \dots, a_M \subset \mathcal{A}$, such that $|a_n| = |a_m|$, $a_n \cap a_m = \emptyset, \forall n, m \in \mathcal{M} := \{1, \dots, M\}, n \neq m$, and $\bigcup_{i=1}^M a_i = \mathcal{A}$. To construct these regions, we adopt an equal-angle discretization of the spherical surface, parameterized by an integer \bar{m} . The sphere is divided into \bar{m} segments along the polar angle $\theta \in [0, \pi]$ and \bar{m} segments along the azimuth angle $\varphi \in [0, 2\pi]$, resulting in $M = \bar{m}^2$ disjoint subregions. For each drone position \mathbf{p} , its spherical coordinates (θ, φ) are computed, and the corresponding subregion index is obtained by uniformly quantizing both angular dimensions into m intervals.

2.2.3. FD calibration. With the above definition, we can obtain a set of flow-density $(q_a, k_a), a \subset \mathcal{A}$. Based on these data, an FD curve can then be developed via regression, following one of the well-known functional specifications such as those of [Greenshields \(1935\)](#), [Greenberg \(1959\)](#), [Drake \(1967\)](#). In this study, Drake’s model ([Drake 1967](#)) is selected due to its smoothness, empirical robustness in congested regimes, and suitability for regression under noisy measurements. Specifically, Drake’s model assumes that the flow-density relationship is

$$q(k) = kv_f e^{-\alpha k}. \quad (4)$$

where v_f is the free-flow speed and $\alpha > 0$ is a decay parameter determined from data.

2.3. Drone control laws

In traffic flow theory, the control law defines the microscopic behavior of individual vehicles as they interact with one another and respond to environmental constraints. The macroscopic properties characterized by the FD are therefore intrinsically determined by these microscopic rules. In the context of UAM, drone behavior in congested environments, such as deceleration, yielding, or rerouting, is primarily dictated by collision-avoidance strategies. Accordingly, the control laws examined in this study explicitly focus on collision-avoidance mechanisms.

Although the robotics community has developed a wide range of collision-avoidance algorithms for UAV ([Rezaee et al. 2024](#)), these methods are largely designed for emergent, local obstacle-avoidance scenarios and focus on guaranteeing safety for individual drones. In contrast,

almost no studies have investigated avoidance strategies from a traffic-control perspective, where collective behavior and macroscopic performance are of primary interest. Because this study aims to examine the macroscopic properties of UAM traffic flow, we consider two control laws inspired by unsignalized intersection management: a stop-and-yield strategy and a circular-detour strategy, following the ideas of the stop-sign and the roundabout operations, respectively. As shown in Figure 1(c), the spacing between drone i and drone $j \in \mathcal{I}$ at time t is denoted by $h_{ijt} = \|\mathbf{p}_{it} - \mathbf{p}_{jt}\|$. For both control laws, a predefined safe spacing \hat{h} is used to identify potential conflicts. A potential collision between drones i and j is considered to occur at time $t \in \mathcal{T}$ whenever $h_{ijt} \leq \hat{h}$. Then, we present the details of the two control laws.

The first control law is the *stop-and-yield strategy*, which mimics stop-sign behavior. Once a potential collision is detected, one of the two drones halts and waits until their spacing again exceeds \hat{h} . Unlike ground transportation systems, UAM operations lack fixed intersection locations, making it impossible to determine right-of-way based on arrival order. To avoid situations in which multiple drones wait for one another, a priority rule is introduced: the lower-priority drone yields to the higher-priority one. For simplicity, priorities in this study are assigned using drone indices. In practical implementations, however, priorities could be determined dynamically based on drone states such as positions, velocities, and OD information, or could be randomized to emulate decentralized conflict resolution without predefined rules.

The second control law is the *circular-detour strategy*, inspired by the operation of roundabouts in roadway systems. When a potential collision is detected between two drones, a virtual circular roundabout is implicitly formed in the local neighborhood, and the drones resolve the conflict by rotating their intended directions while maintaining continuous flight. At time t , if drone i is navigating toward its destination \mathbf{p}_{in}^D , its nominal direction of motion is given by the unit vector $\mathbf{d}(\mathbf{p}_{it}, \mathbf{p}_{in}^D)$. To explore alternative rotation directions, this nominal direction is rotated around the outward normal $\hat{\mathbf{p}}_{it} = \mathbf{p}_{it} / \|\mathbf{p}_{it}\|$ using Rodrigues rotations (Piña 2011). A set of candidate rotation angles Ψ is generated by uniformly sampling the interval $(0, 2\pi)$. For each sampled angle $\psi \in \Psi$, the rotated direction is obtained as

$$\mathbf{d}_{\text{rot}}(\psi) = \mathbf{d}(\mathbf{p}_{it}, \mathbf{p}_{in}^D) \cos \psi + (\hat{\mathbf{p}}_{it} \times \mathbf{d}(\mathbf{p}_{it}, \mathbf{p}_{in}^D)) \sin \psi + \hat{\mathbf{p}}_{it} (\hat{\mathbf{p}}_{it} \cdot \mathbf{d}(\mathbf{p}_{it}, \mathbf{p}_{in}^D)) (1 - \cos \psi), \quad (5)$$

followed by normalization to maintain step length. A candidate angle ψ is considered safe if $\mathbf{d}_{\text{rot}}(\psi) \cdot \mathbf{d}(\mathbf{p}_{it}, \mathbf{p}_{jt}) \leq 0$ for all neighbors j , ensuring that the rotated direction does not move the drone closer to any conflict drone. Among all safe candidates, the one maximizing $\mathbf{d}_{\text{rot}}(\psi) \cdot \mathbf{d}(\mathbf{p}_{it}, \mathbf{p}_{in}^D)$ is selected, resulting in the smallest deviation from the nominal direction.

Figure 4 illustrates how the two control laws resolve potential collisions in a simple example. In Figure 4(a), the left drone i has lower priority and therefore, after following the solid trajectory

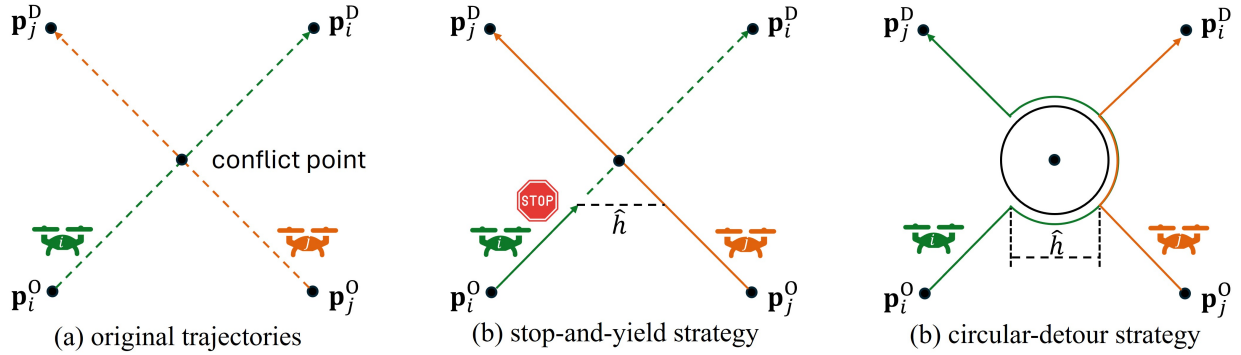


Figure 4 An example of the stop-and-yield and circular-detour strategies.

segment, it yields to drone j and waits until drone j passes, before continuing along the dashed trajectory toward its destination. In Figure 4(b), drones i and j both enter a virtual roundabout constructed between them and travel along circular detour paths to avoid collision.

2.4. Algorithm overview

With all the components described in the previous sections, this subsection summarizes the overall procedures for UAM traffic simulation and FD calibration. Algorithm 1 outlines the UAM traffic simulation pipeline, which iteratively updates drone states according to OD assignments and the specified control laws, thereby generating full-trajectory datasets. Using these simulated trajectories, we can directly obtain the corresponding FD of the simulated traffic flow. Algorithm 2 then converts the trajectory data into macroscopic flow–density measurements by computing Edie-based density and flow over the spherical subregions and subsequently fitting the FD. In addition to simulation-based FD construction, the same procedure in Algorithm 2 can be applied to the real-world flight trajectories collected through the physical tests presented in the next section, yielding the empirical FD of real UAM traffic.

3. Experiment design for data collection

This section introduces the reduced-scale UAM testbed and the collected UAMTra2Flow dataset.

3.1. Reduced-scale UAM testbed

physical tests were conducted using a reduced-scale experimental platform based on the Bitcraze Crazyflie 2.1+. Crazyflie 2.1+ is a versatile development platform for aerial robotics research and has been widely used in laboratory-based drone studies, as reported in the literature (Preiss et al. 2017, Duisterhof et al. 2021, Hegde et al. 2024).

3.1.1. Hardware Setup. Our hardware setup includes a personal computer equipped with a 3.2 GHz AMD Ryzen 7 7735HS CPU with Radeon Graphics and 16 GB of RAM, running the Ubuntu 22.04 operating system. Equipped with a Crazyradio 2.0, the computer is able to establish

Algorithm 1 UAM Traffic Simulation Framework

- 1: **Input:** number of drones I , time step Δt , maximum steps T , speed \bar{v} , safe spacing \hat{h} , scenario type, control law type.
 - 2: **for all** $i \in \mathcal{I}$ **do**
 - 3: Generate OD pairs $\{(\mathbf{p}_{in}^O, \mathbf{p}_{in}^D)\}$ according to the scenario type.
 - 4: Initialize drone position \mathbf{p}_{i0} .
 - 5: **end for**
 - 6: **for all** $t \in \mathcal{T}$ **do**
 - 7: **for all** $i \in \mathcal{I}$ **do**
 - 8: Log each drone's current position \mathbf{p}_{it} and destination \mathbf{p}_{in}^D .
 - 9: Compute distances $h_{ijt} = \|\mathbf{p}_{it} - \mathbf{p}_{jt}\|$ to neighboring drones.
 - 10: **if** $\min_j h_{ijt} \leq \hat{h}$ **then**
 - 11: **if** control law = stop-and-yield **then**
 - 12: Drone i stops at \mathbf{p}_{it} .
 - 13: **else if** control law = circular-detour **then**
 - 14: Generate the set of candidate rotation angles Ψ by uniformly sampling $(0, 2\pi)$.
 - 15: For each $\psi \in \Psi$, compute the rotated direction $\mathbf{d}_{rot}(\psi)$ using Eq. (5).
 - 16: Select the angle $\psi^* = \arg \max_{\psi \in \Psi} \mathbf{d}_{rot}(\psi) \cdot \mathbf{d}(\mathbf{p}_{it}, \mathbf{p}_{in}^D)$ s.t. $\mathbf{d}_{rot}(\psi) \cdot \mathbf{d}(\mathbf{p}_{it}, \mathbf{p}_{jt}) \leq 0, \forall j \in \mathcal{I}$.
 - 17: Move drone i along $\mathbf{d}_{rot}(\psi^*)$.
 - 18: **end if**
 - 19: **else**
 - 20: Move toward \mathbf{p}_{in}^D via nominal slerp step.
 - 21: **end if**
 - 22: Terminate if drone i reach final destination \mathbf{p}_{in}^D .
 - 23: **end for**
 - 24: **end for**
 - 25: **Output:** drone trajectories $\{\mathbf{p}_{it}\}$ and OD pairs $\{(\mathbf{p}_{in}^O, \mathbf{p}_{in}^D)\}$.
-

wireless communication with each Crazyflie, enabling real-time command transmission and data collection.

To obtain accurate position estimates, we use the Bitcraze-recommended indoor localization system based on lighthouse stations. The drones operate on a spherical surface of radius 1 m. To ensure that the lighthouse system can reliably capture drone positions within this flight envelope, four lighthouse stations are installed at the four corners of a 3 m \times 3 m rectangular area,

Algorithm 2 FD Construction from Simulation or Experimental Data

- 1: **Input:** trajectories $\{\mathbf{p}_{it}\}$, destinations $\{\mathbf{p}_{in}^D\}$, region partition $\{a_m\}_{m \in \mathcal{M}}$ on \mathcal{A} , time step Δt , total steps T , number of bins B , percentile level p .
 - 2: Initialize $t_{iam} \leftarrow 0$, $s_{iam} \leftarrow 0$ for all drones $i \in \mathcal{I}$ and regions $m = 1, \dots, M$.
 - 3: **for all** $i \in \mathcal{I}$ **do**
 - 4: Segment the trajectory of drone i into intervals with fixed destination \mathbf{p}_{in}^D .
 - 5: **for all** $t \in \mathcal{T}$ **do**
 - 6: Determine region index m such that $\mathbf{p}_{it} \in a_m$.
 - 7: Update time spent in region a_m : $t_{iam} \leftarrow t_{iam} + \Delta t$.
 - 8: Accumulate effective distance in region a_m : $s_{iam} \leftarrow s_{iam} + \Delta s_{it}$ by Eq. (3).
 - 9: **end for**
 - 10: **end for**
 - 11: Compute density and flow pairs $\{(k_{am}, q_{am})\}_{m \in \mathcal{M}}$ by Eqs. (1)–(2).
 - 12: Divide the range of $\{k_{am}\}$ into B equal-width density bins.
 - 13: **for all** $b \in \mathcal{B}$ **do**
 - 14: Let $\mathcal{M}_b = \{m : k_{am} \text{ falls into bin } b\}$.
 - 15: **if** $\mathcal{M}_b \neq \emptyset$ **then**
 - 16: Compute flow threshold q_b^{thr} as the p -th percentile of $\{q_{am} : m \in \mathcal{M}_b\}$.
 - 17: Keep only samples with $q_{am} \geq q_b^{\text{thr}}$ in bin b .
 - 18: **end if**
 - 19: **end for**
 - 20: Fit Drake’s model in Eq. (4) to all retained (k_{am}, q_{am}) via least square to obtain FD parameters.
 - 21: **Output:** FD parameters.
-

each mounted at a height of approximately 2.5 m. Each Crazyflie is equipped with a positioning deck that receives signals from the lighthouse stations and computes its 3D position. This setup enables robust and precise localization throughout the test space. The hardware configuration is summarized in Figure 5.

3.1.2. Software Architecture. To achieve accurate control of the drone swarm, we employ the ROS 2-based Python package *Crazyswarm2* (Kaufmann et al. 2023). Developed by the Intelligent Multi-Robot Coordination Lab, *Crazyswarm2* is an open-source software framework specifically designed for controlling swarms of Bitcraze Crazyflie drones. It offers a comprehensive set of APIs that allow users to implement multi-drone control using Python scripts.

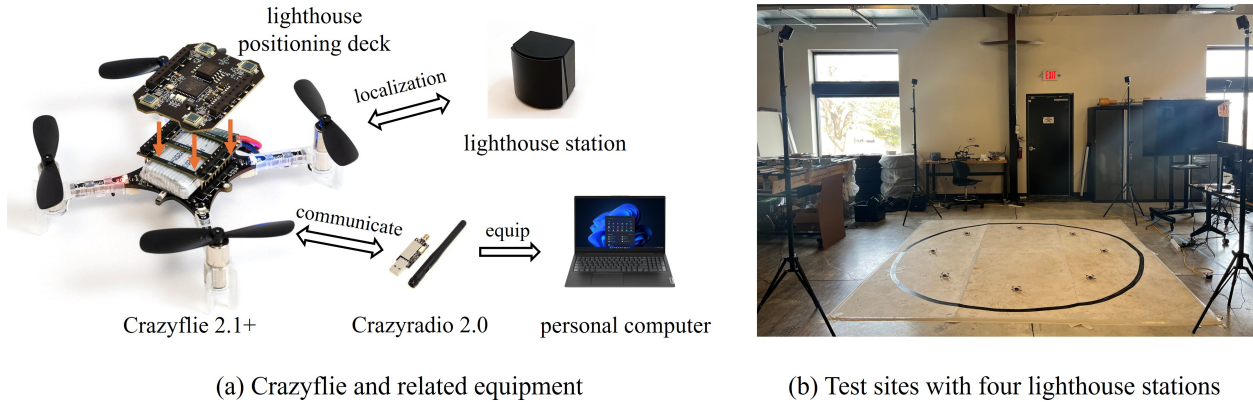


Figure 5 Hardware setup for the reduced-scale testbed and the deployment of the indoor test site.

Building on the ROS 2 middleware and the CrazySwarm2 framework, we developed a multi-process control architecture for coordinated trajectory tracking of multiple drones. This design ensures modularity, high-frequency command execution, and safe parallel operations across the drone swarm. The overall software architecture is illustrated in Figure 6. The system consists of four main types of nodes:

- **WaypointLoaderNode**: loads predefined waypoint trajectories from CSV files and publishes them to the corresponding commanders via mission topics.
- **SingleCfCommander**: controls one drone by receiving its assigned waypoints and sending either high-frequency position commands or discrete movement requests to the backend. Each drone is associated with one independent commander process.
- **Crazyflie Backend**: serves as the communication interface between the ROS 2 network and the physical Crazyflie drones, providing services for takeoff, movement, and landing, as well as pose feedback.
- **TrajectoryLoggerNode**: subscribes to all drone pose topics and records the flight trajectories for post-experiment evaluation and analysis.

Based on this structure, a multi-process implementation is adopted instead of a multi-threaded one to avoid potential deadlocks in concurrent callback execution, which are common in ROS 2 multi-threading. Moreover, running each drone controller in an independent process ensures real-time responsiveness, allowing all drones to receive high-frequency control commands simultaneously without interference or scheduling delays.

3.2. UAM trajectory-based traffic flow dataset

Following the methodology introduced in Section 2 and the physical test setup described in Section 3.1, we collect a trajectory-based UAM traffic flow dataset, **UAMTra2Flow**. The dataset consists of two components: (i) simulation data and (ii) physical test data, representing drone

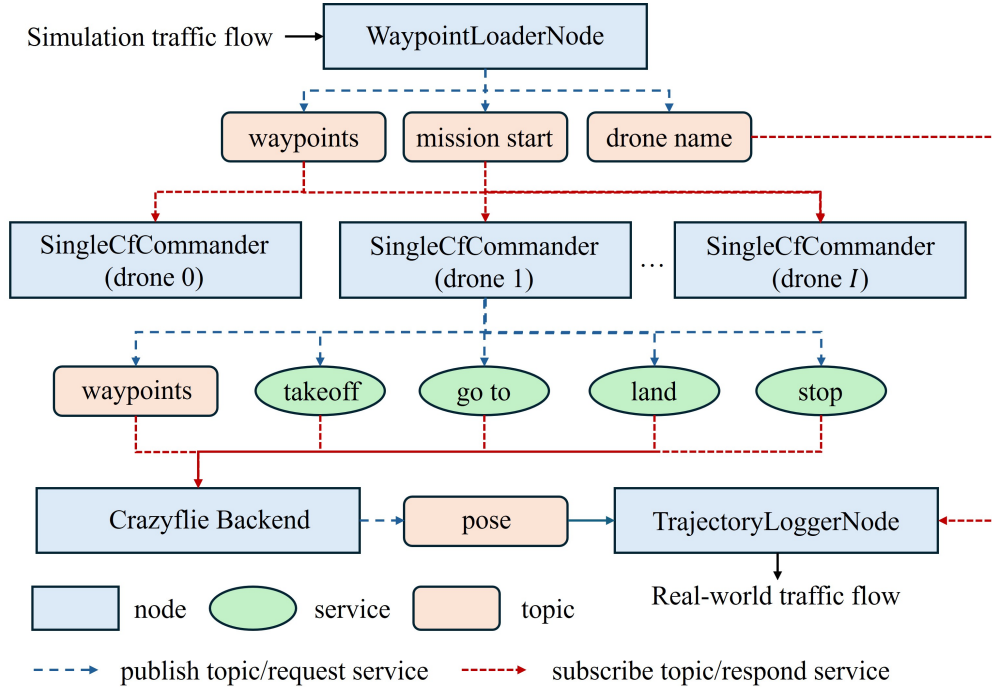


Figure 6 System architecture for drone swarm control using ROS 2 and Crazyswarm2.

trajectories generated by the simulation framework and collected from real-world physical tests, respectively. The physical test component contains approximately 46 minutes of flight trajectories, corresponding to about 140,000 rows of CSV-formatted data. The dataset is publicly available at <https://github.com/CATS-Lab/UAM-FD>. **The source code will be released upon acceptance of this paper.**

In the UAMTra2Flow dataset, we collect physical test data for two control laws across three scenario types. For each control law, two safety spacing settings are considered: for the stop-and-yield strategy, $\hat{h} \in \{0.5, 0.6\}$ m; for the circular-detour strategy, $\hat{h} \in \{0.6, 0.7\}$ m. To ensure that the collected data cover both free-flow and congested traffic regimes and thus enable reliable FD construction, experiments are conducted with different drone fleet sizes, $I \in \{2, 4, 6, 8\}$, for each configuration. In the physical tests, each configuration is ran once for each drone number, resulting in a total of 48 traffic flow trajectory segments. To obtain a larger number of data samples, each configuration in simulation is repeated four times, yielding 192 traffic flow trajectory segments in total. In addition, readers can generate further simulation data or collect additional physical test trajectories using the released codebase.

Due to battery limitations, each test run lasts approximately 60 s, including 5 s for takeoff, 50 s of steady flight, and 3 s for landing. Trajectories are recorded at a sampling interval of $\Delta t = 0.1$ s, and the desired cruising speed is set to $\bar{v} = 0.5$ m/s. To prevent drones from completing all assigned

Table 1 Structure of the UAMTra2Flow dataset.

Column Name	Description	Unit
id	Drone ID	N/A
time	Timestamp ($\Delta t = 0.1$ s)	s
px	x -coordinate of drone position	m
py	y -coordinate of drone position	m
pz	z -coordinate of drone position	m
dest_px	x -coordinate of current destination	m
dest_py	y -coordinate of current destination	m
dest_pz	z -coordinate of current destination	m

flights prematurely, which would bias traffic flow measurements, we assign a sufficiently large number of OD flights N so that all drones remain active throughout the experiment duration.

All trajectory data are stored in CSV files, with the column definitions summarized in Table 1. In particular, the dataset records both the drone’s current position and the coordinates of its next destination, which are required for computing the effective distance used in the FD analysis.

4. Experiment results and discussions

This section presents the construction and analysis of the FDs using both the simulation data and the physical test data collected in Section 3.2. The results obtained from the different control laws and different scenario types are compared to evaluate the traffic characteristics of UAM. Finally, we scale the FD parameters to realistic conditions.

4.1. Calibration of the FDs

Using the UAMTra2Flow dataset, we calibrate the FD following the procedure described in Algorithm 2. Prior to computing density and flow, only the trajectories recorded during the steady-flight phase are considered, while the takeoff and landing segments are excluded. Moreover, to ensure that the analysis reflects stable traffic conditions, the first 15 seconds of the steady-flight trajectories are further removed from the FD calibration.

For the calibration, the spherical partition parameter is set to $\bar{m} = 7$, yielding $M = 128$ spatial subregions on the spherical surface. The calibrated FD parameters, together with the corresponding goodness-of-fit metrics including R^2 and RMSE, are summarized in Table 2. The flow–density data points and the fitted FD curves for both simulation and physical experiments are illustrated in Figures 7–8.

In Table 2, q_{\max} denotes the maximum flow rate (unit: $\text{m}^{-1}\text{s}^{-1}$), k_c (unit: m^{-2}) represents the critical density, and v_f (unit: ms^{-1}) is the free-flow speed. Based on the R^2 and RMSE values, the regression models exhibit overall strong performance when compared with related studies Shi and Li (2021). For simulation, all calibrated models achieve R^2 values above 0.5, with RMSE

Table 2 Fitted parameters and calibration results of Drake's model. Here, stop refers to the stop-and-yield strategy, and detour refers to the circular-detour strategy.

Scenario type	Control law	Experiment type	\hat{h} (m)	q_{\max} ($\text{m}^{-1}\text{s}^{-1}$)	k_c (m^{-2})	v_f (m s^{-1})	R^2	RMSE (m s^{-1})
scenario 1	stop	simulation	0.5	0.251	0.966	0.429	0.664	0.050
			0.6	0.171	0.671	0.420	0.563	0.044
		physics	0.5	0.221	1.045	0.349	0.643	0.048
	0.6		0.104	0.590	0.291	0.328	0.041	
	0.6		0.258	1.164	0.366	0.610	0.055	
	detour	simulation	0.7	0.213	0.975	0.360	0.609	0.049
0.6			0.188	1.011	0.307	0.561	0.052	
physics		0.7	0.176	0.830	0.349	0.615	0.041	
scenario 2	stop	simulation	0.5	0.224	1.064	0.347	0.705	0.043
			0.6	0.152	0.688	0.363	0.571	0.039
		physics	0.5	0.205	1.271	0.266	0.668	0.038
	0.6		0.134	0.760	0.290	0.533	0.035	
	0.6		0.296	1.531	0.318	0.791	0.044	
	detour	simulation	0.7	0.199	0.977	0.335	0.700	0.042
0.6			0.225	1.480	0.251	0.782	0.038	
physics		0.7	0.160	1.018	0.259	0.632	0.037	
scenario 3	stop	simulation	0.5	0.256	0.994	0.425	0.627	0.057
			0.6	0.176	0.673	0.431	0.532	0.049
		physics	0.5	0.186	0.738	0.415	0.448	0.058
	0.6		0.157	0.747	0.347	0.485	0.046	
	0.6		0.258	1.071	0.398	0.676	0.055	
	detour	simulation	0.7	0.209	1.047	0.329	0.530	0.060
0.6			0.217	0.971	0.368	0.579	0.051	
physics		0.7	0.200	1.022	0.322	0.543	0.060	

below 0.06. In comparison, the calibration results obtained from physical test are slightly less accurate; nevertheless, most cases still attain R^2 values above 0.45 and RMSE below 0.06. These results suggest that traditional FD models originally developed for ground transportation remain effective for characterizing the macroscopic traffic behavior of UAM systems.

Besides, for both Table 2 and Figure 7-8, we can also observe that there are noticeable differences between the FD curves obtained from simulation and physical test. Specifically, the FD curves derived from physical tests typically exhibit lower free-flow speeds and smaller maximum flows compared to those obtained from simulations. Furthermore, the data from physical tests fit less well in general. These differences are likely due to various uncertainties in the physical tests, such as air resistance and communication delay between the base stations and drones. Air resistance slightly reduces the actual drone speed as relative to the desired speed, while communication delay decreases the responsiveness to position and speed commands. This finding suggests the importance of corroborating theoretical or simulation results with physical tests.

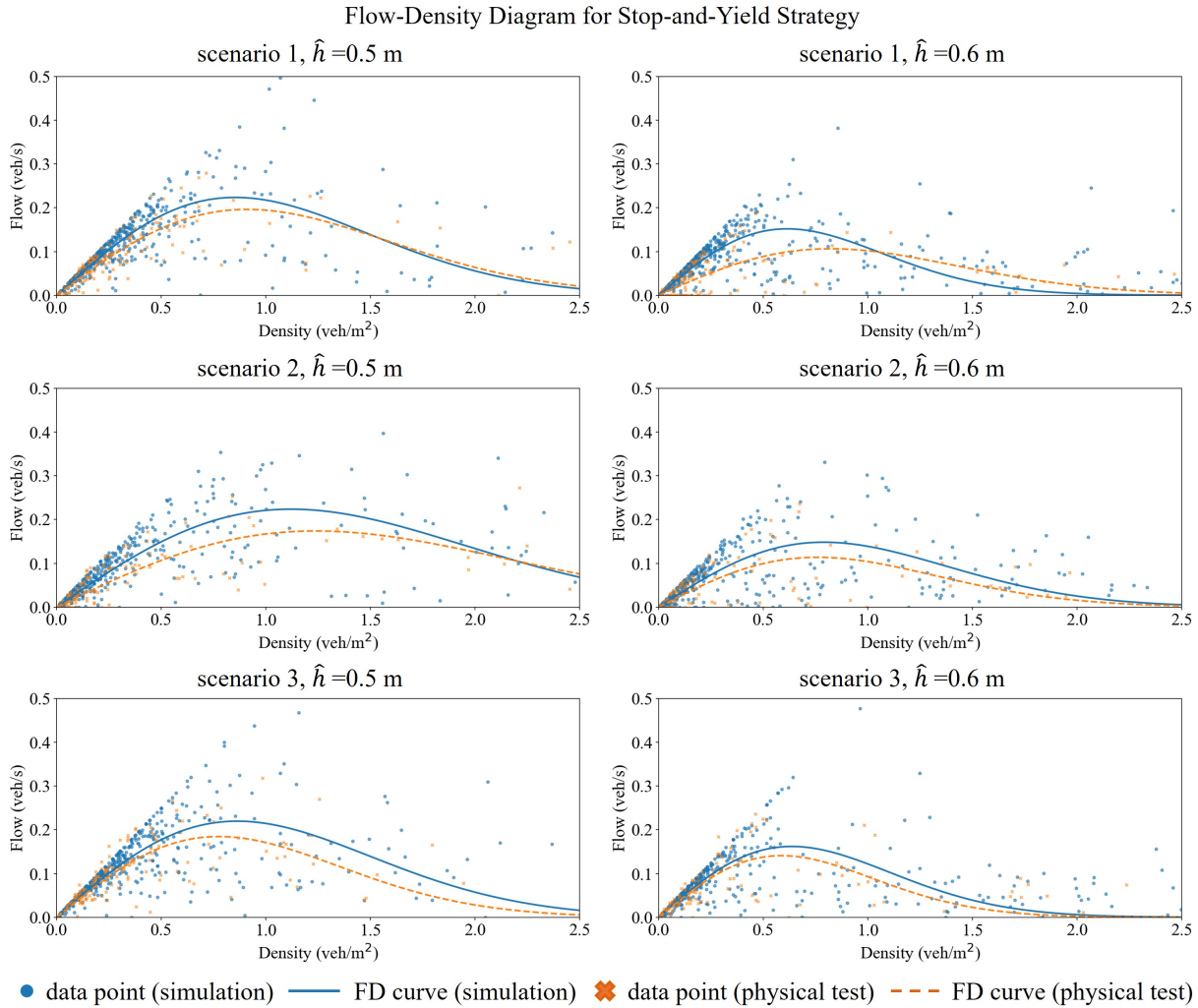


Figure 7 FD plots for simulation and physical tests for stop-and-yield strategy.

4.2. Comparison between different control laws

To compare the characteristics of different control laws, we plot the FD curves obtained under the stop-and-yield strategy and the circular-detour strategy in Figure 9. When comparing the same control law under different safety spacing settings, a clear pattern emerges: larger safety spacing consistently leads to a lower maximum flow. This observation indicates that traffic capacity, defined as the maximum achievable flow rate, decreases as the safety spacing increases, which is consistent with well-established findings in ground transportation systems.

However, the relationship between safety spacing and critical density varies across scenarios. In Scenario 1, different safety spacing settings yield similar critical densities, whereas in Scenarios 2 and 3, a larger safety spacing is associated with a higher critical density. This suggests that the impact of safety spacing on the location of the critical point depends on the underlying traffic scenario and interaction patterns.

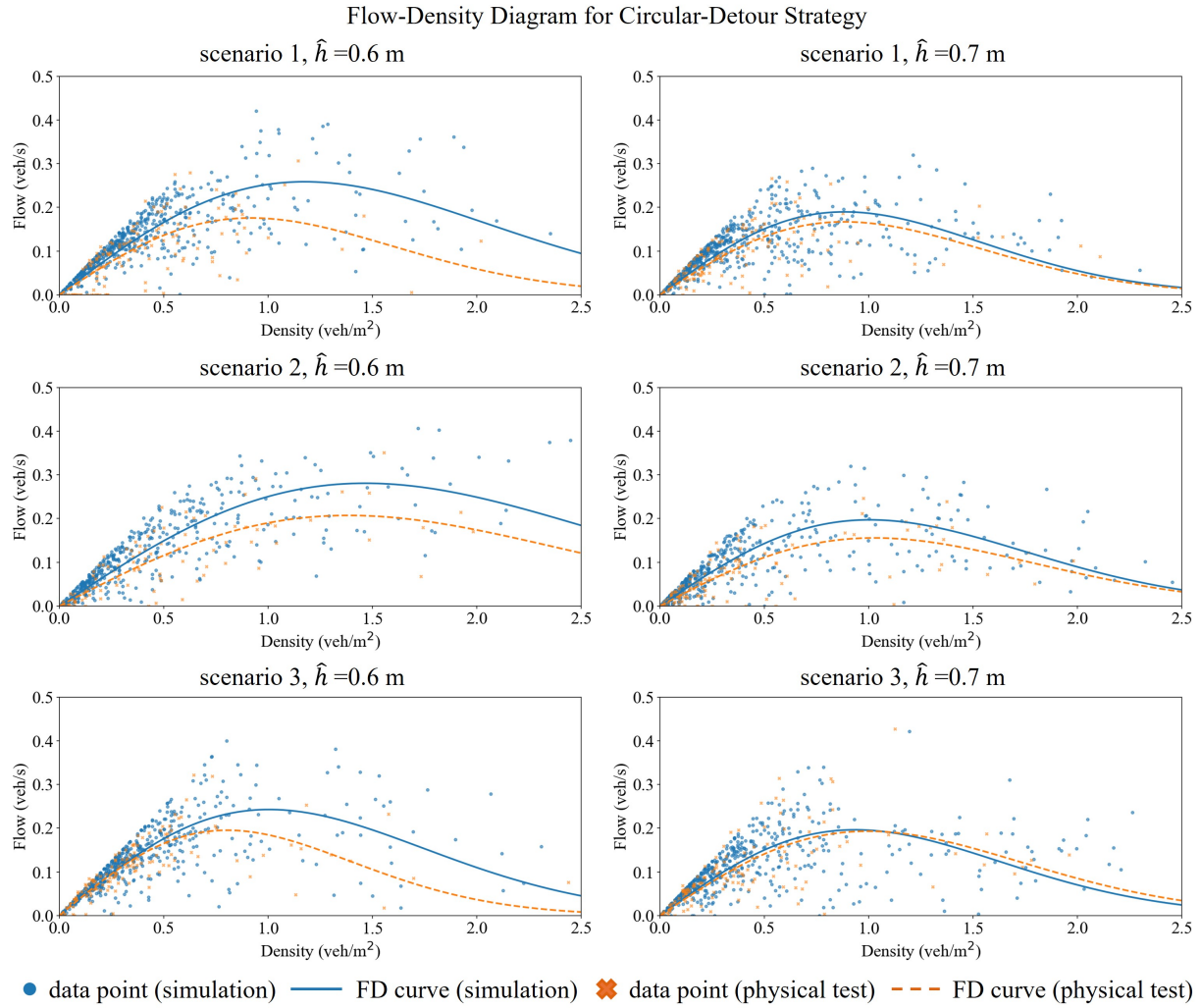


Figure 8 FD plots for simulation and physical tests for circular-detour strategy.

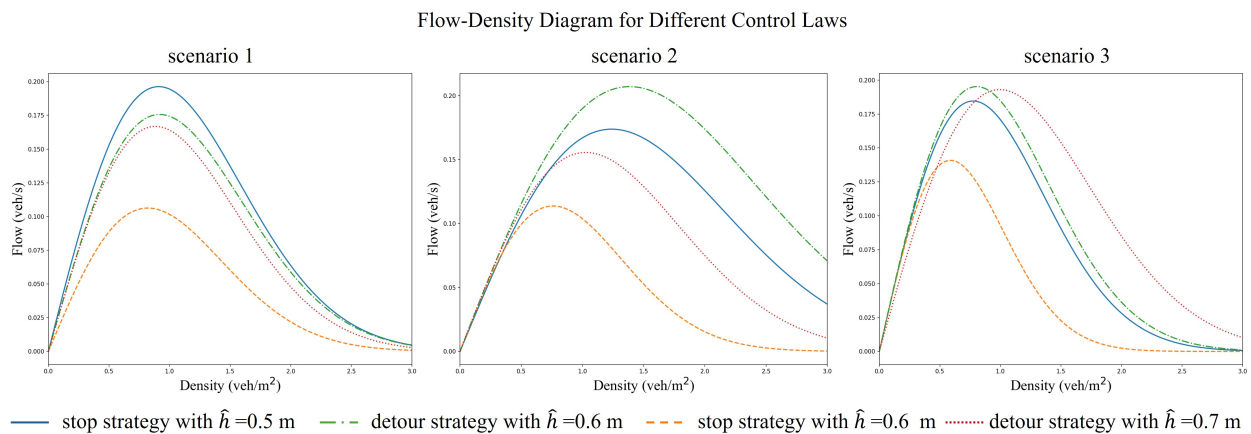


Figure 9 FD plots for the stop-and-yield strategy and the circular-detour strategy with different safety spacing.

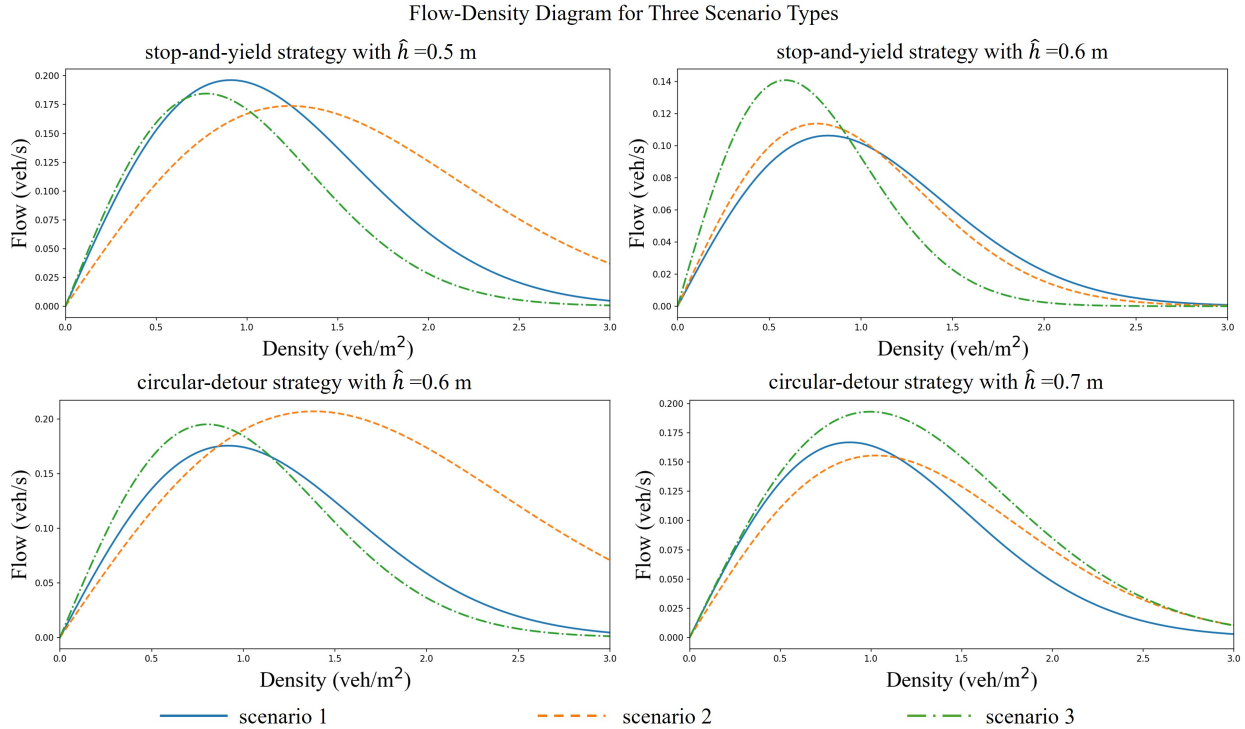


Figure 10 FD plots for comparison for three scenario types.

When comparing different control laws under the same safety spacing setting, the circular-detour strategy consistently produces a higher maximum flow rate, indicating superior traffic capacity. A plausible explanation is that the circular-detour strategy allows drones involved in potential conflicts to maintain continuous motion by dynamically adjusting their directions, thereby preventing the formation of localized blockages. In contrast, under the stop-and-yield strategy, once multiple drones accumulate near a conflict region, low-priority drones may remain stationary for extended periods, which amplifies congestion and substantially reduces throughput.

Finally, we observe that both control laws exhibit similar free-flow speeds across different safety spacing settings, with the only notable exception being the stop-and-yield strategy with $\hat{h} = 0.6$ m in Scenario 1. This overall consistency in free-flow speed supports the effectiveness of the proposed effective-distance measurement, which preserves accurate flow estimation in the uncongested regime.

4.3. Comparison between different application scenarios

Figure 10 compares the FD curves across different scenario types. Overall, no single scenario consistently dominates the others in terms of congestion level, as the relative traffic performance varies depending on the control law and safety spacing settings. Nevertheless, a general trend can be observed: Scenario 3 tends to exhibit less severe congestion compared with the other

two scenario types. A plausible explanation is that Scenario 3 represents station-to-station operations between fixed locations, where drone trajectories are more structured and recurrent, effectively forming lane-like patterns in the airspace. In contrast, in Scenarios 1 and 2, where origin–destination pairs are generated randomly, drone movements are more disordered, which increases interaction complexity and makes congestion more likely to occur.

4.4. Scaling to real-world UAM

To bridge the gap between reduced-scale physical experiments and real-world UAM operations, we attempt to scale the calibrated FD parameters to realistic operational settings. We assume that the macroscopic FD is mainly governed by the characteristic cruising speed and the effective spatial occupancy induced by vehicle size and safety spacing. Under this assumption, traffic density scales with the inverse of the occupied area, while traffic flow scales linearly with the characteristic speed.

Let η and η' denote the characteristic length of a drone in the reduced-scale testbed and in the realistic operational setting, respectively, and let \bar{v}' denote the desired cruising speed in the realistic setting. Define the scaling factors for size and speed as $\delta_\eta := \frac{\eta'}{\eta}$ and $\delta_v := \frac{\bar{v}'}{\bar{v}}$. In our FD, density is measured in veh/m^2 and flow in $\text{veh}/(\text{m} \cdot \text{s})$, so the scaled FD parameters can be expressed as

$$v'_f = v_f \delta_v, \quad k'_c = \frac{k_c}{\delta_\eta^2}, \quad q'_{\max} = q_{\max} \frac{\delta_v}{\delta_\eta^2}, \quad (6)$$

In the experiments, the Crazyflie drone has a footprint of approximately $10 \text{ cm} \times 10 \text{ cm}$, and thus we take $\eta = 10 \text{ cm}$. Referring to the specifications of a representative large-scale UAM vehicle, the DJI FlyCart 100 (DJI 2024), we set the realistic drone size to $\eta' = 2 \text{ m}$ and cruising speed $\bar{v}' = 10 \text{ m/s}$. Using these parameters, the calibrated FD results in Table 2 are scaled to realistic UAM settings, as reported in Table 3. Here, \hat{h}' denotes the scaled safety spacing, with units of m. For ease of comparison with real-world data, all other FD parameters are converted to a km–h unit system.

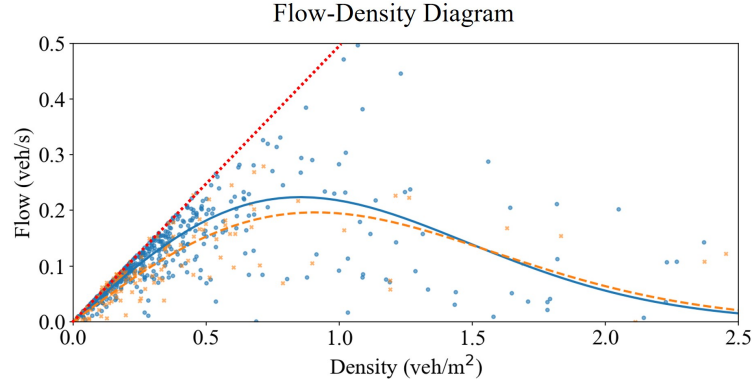
4.5. Limitation

Although the R^2 and RMSE values indicate that the FD calibration is reasonably accurate, Table 2 shows that the estimated free-flow speed is consistently lower than the desired cruising speed $\bar{v} = 0.5 \text{ m/s}$. This discrepancy arises because the measured regions may contain mixed traffic states, including both free-flow and congested conditions, as discussed in Section 2.2.2. While the partitioning procedure helps mitigate this effect, it may not fully eliminate it. As a result, the current FD calibration may exhibit some bias, which can be regarded as a limitation of this study.

However, by examining Figures 7–8, we observe that although the calibrated free-flow speed in the FD is lower than \bar{v} , the upper envelope of the data points still forms a clear linear trend with

Table 3 FD parameters scaled to realistic UAM operations.

Scenario type	Control law	\hat{h}' (m)	q'_{\max} ($\text{km}^{-1}\text{h}^{-1}$)	k'_c (km^{-2})
scenario 1	stop	10	38520	2602.5
		12	18360	1462.5
	detour	12	31140	2297.5
		14	30780	1992.5
scenario 2	stop	10	35460	3310.0
		12	19440	1610.0
	detour	12	41040	3997.5
		14	28800	2565.0
scenario 3	stop	10	32220	1932.5
		12	24300	1447.5
	detour	12	37620	2282.5
		14	35100	2567.5



● data point (simulation) — FD curve (simulation) ✕ data point (physical test) - - - FD curve (physical test)
 Upper envelope line of data points with density less than 1.0

Figure 11 Illustration of the upper envelope of the flow–density data points.

a slope close to \bar{v} , as illustrated in Figure 11. This suggests that data points representing mixed traffic states are more likely to be distributed inside the FD rather than along its upper boundary. If traffic-flow-theory-based filtering methods are applied to remove unreasonable flow–density data points, the accuracy of FD calibration could be further improved. By releasing the UAMTra2Flow dataset and the associated code, we believe this study can effectively support future research in this direction.

5. Conclusion and future research

This study presents a general framework for constructing the FD of UAM traffic flow using both simulation and physical experiments. From the theoretical perspective, the proposed framework integrates UAM traffic definitions, control law design, and traffic flow theory to generate UAM traffic flows and characterize the relationship between drone density and traffic flow under

diverse operational conditions. From the experimental perspective, a reduced-scale UAM testbed based on Crazyflie drones and the ROS 2 system is established to enable accurate drone control and reliable trajectory data collection, thereby supporting real-world UAM traffic flow analysis. Based on the proposed framework, the UAMTra2Flow dataset is collected, which can facilitate future studies on UAM traffic modeling and management. Analysis of the FDs derived from the UAMTra2Flow dataset confirms that classical traffic flow patterns developed for ground transportation are largely applicable to UAM systems, while also revealing systematic deviations from simulation-based results. These findings underscore the importance of incorporating physical experiments in UAM traffic studies to better capture real-world system dynamics. Moreover, the results demonstrate that different control laws have distinct impacts on UAM traffic performance, motivating the design of appropriate control strategies for efficient and reliable UAM traffic operations.

Although the proposed framework has been preliminarily validated, several limitations remain. First, the number of experimental runs is limited, which constrains the extent to which the effects of control parameters and modeling assumptions can be systematically analyzed. Second, despite incorporating both theoretical analysis and physical experiments, the current study still relies on certain simplifications. For example, the control laws are considered with fixed safety spacing, where in the reality the safety spacing might be different according to the current speed. These simplification may result that the current experiment not capture the full diversity and variability of future UAM systems. Finally, as discussed in Section 4.5, the unique characteristics of UAM traffic may require dedicated FD calibration methods to further improve accuracy. Future work can be conducted along several directions. First, the number of experimental scenarios can be expanded to support more comprehensive analyses. Second, more realistic operational scenarios and control laws can be designed to better reflect real-world UAM operations. Finally, advanced filtering or data-selection methods for flow–density observations can be explored to improve FD calibration accuracy. These efforts will further enhance the applicability of FD-based approaches in guiding UAM traffic management and infrastructure development.

References

- Ambühl L, Loder A, Bliemer MC, Menendez M, Axhausen KW (2020) A functional form with a physical meaning for the macroscopic fundamental diagram. *Transportation Research Part B: Methodological* 137:119–132.
- Amirgholy M, Gao HO (2017) Modeling the dynamics of congestion in large urban networks using the macroscopic fundamental diagram: User equilibrium, system optimum, and pricing strategies. *Transportation Research Part B: Methodological* 104:215–237.

-
- Battista A, Ni D (2017) Modeling small unmanned aircraft system traffic flow under external force. *Transportation Research Record* 2626(1):74–84.
- Bilion W, Wu N, Schmitz J (2023) Fundamental diagram for an intersection: application for a roundabout. *Transportation Research Record* 2677(7):359–372.
- CCTV (2024) Low-altitude economy gains momentum: How can drones fly further and more stably? URL <https://news.cctv.com/2024/12/01/ARTIogziPhG331m9UeVcR60K241201.shtml>, accessed: 2025-09-29.
- Cummings C, Mahmassani H (2021) Emergence of 4-d system fundamental diagram in urban air mobility traffic flow. *Transportation Research Record* 2675(11):841–850.
- Cummings C, Mahmassani H (2024) Comparing urban air mobility network airspaces: Experiments and insights. *Transportation Research Record* 2678(4):440–454.
- Cummings C, Mahmassani HS (2023) Measuring the impact of airspace restrictions on air traffic flow using four-dimensional system fundamental diagrams for urban air mobility. *Transportation Research Record* 2677(1):1012–1026.
- Daamen W, Hoogendoorn S, Bovy P (2005) First-order pedestrian traffic flow theory. *PHL* 1:1–14, URL <http://dx.doi.org/10.3141/1934-05>.
- Daganzo CF, Geroliminis N (2008) An analytical approximation for the macroscopic fundamental diagram of urban traffic. *Transportation Research Part B: Methodological* 42(9):771–781.
- DJI (2024) DJI FlyCart 100 Specifications. <https://www.dji.com/flycart-100/specs>, accessed: 2025-01-19.
- Drake JS (1967) A statistical analysis of speed density hypothesis. *HRR* 154:53–87.
- Duisterhof BP, Krishnan S, Cruz JJ, Banbury CR, Fu W, Faust A, de Croon GC, Reddi VJ (2021) Tiny robot learning (tinyrl) for source seeking on a nano quadcopter. *2021 IEEE International Conference on Robotics and Automation (ICRA)*, 7242–7248 (IEEE).
- Edie L (1963) Discussion of traffic stream measurements and definitions. *Port of New York* .
- Flötteröd G, Lämmel G (2015) Bidirectional pedestrian fundamental diagram. *Transportation Research Part B: Methodological* 71:194–212.
- Frachtenberg E (2019) Practical drone delivery. *Computer* 52(12):53–57.
- Greenberg H (1959) An analysis of traffic flow. *Operations Research* 7(1):79–85.
- Greenshields BD (1935) A study in highway capacity. *Highway Research Board Proc., 1935* 448–477.
- Haddad J, Mirkin B, Assor K (2021) Traffic flow modeling and feedback control for future low-altitude air city transport: An mfd-based approach. *Transportation Research Part C: Emerging Technologies* 133:103380.
- Hegde S, Huang Z, Sukhatme GS (2024) Hyperppo: A scalable method for finding small policies for robotic control. *2024 IEEE International Conference on Robotics and Automation (ICRA)*, 10821–10828 (IEEE).

- Hoogendoorn SP, Daamen W, Knoop VL, Steenbakkens J, Sarvi M (2018) Macroscopic fundamental diagram for pedestrian networks: theory and applications. *Transportation Research Part C: Emerging Technologies* 94:172–184.
- Kaufmann E, Loquercio A, Gehrig M, Ranftl R, Scaramuzza D (2023) CrazySwarm2: Large-scale multi-robot aerial platform. <https://imrclab.github.io/crazyswarm2/index.html>, accessed: 2025-07-16.
- Otto A, Agatz N, Campbell J, Golden B, Pesch E (2018) Optimization approaches for civil applications of unmanned aerial vehicles (uavs) or aerial drones: A survey. *Networks* 72(4):411–458.
- Piña E (2011) Rotations with Rodrigues' vector. *European Journal of Physics* 32(5):1171.
- Preiss JA, Honig W, Sukhatme GS, Ayanian N (2017) CrazySwarm: A large nano-quadcopter swarm. 2017 *IEEE International Conference on Robotics and Automation (ICRA)*, 3299–3304 (IEEE).
- Qu X, Zhang J, Wang S (2017) On the stochastic fundamental diagram for freeway traffic: Model development, analytical properties, validation, and extensive applications. *Transportation Research Part B: Methodological* 104:256–271.
- Rezaee MR, Hamid NAWA, Hussin M, Zukarnain ZA (2024) Comprehensive review of drones collision avoidance schemes: Challenges and open issues. *IEEE Transactions on Intelligent Transportation Systems* 25(7):6397–6426.
- Saberi M, Mahmassani HS (2014) Exploring areawide dynamics of pedestrian crowds: three-dimensional approach. *Transportation Research Record* 2421(1):31–40.
- Saberi M, Mahmassani HS, Hou T, Zockaie A (2014) Estimating network fundamental diagram using three-dimensional vehicle trajectories: extending edie's definitions of traffic flow variables to networks. *Transportation Research Record* 2422(1):12–20.
- Shi X, Li X (2021) Constructing a fundamental diagram for traffic flow with automated vehicles: Methodology and demonstration. *Transportation Research Part B: Methodological* 150:279–292.
- Vanumu LD, Ramachandra Rao K, Tiwari G (2017) Fundamental diagrams of pedestrian flow characteristics: A review. *European Transport Research Review* 9(4):49.
- Wikipedia (2025a) Slerp. URL <https://en.wikipedia.org/wiki/Slerp>.
- Wikipedia (2025b) Spherical law of cosines. URL https://en.wikipedia.org/wiki/Spherical_law_of_cosines.
- Wu N (2002) A new approach for modeling of fundamental diagrams. *Transportation Research Part A: Policy and Practice* 36(10):867–884.
- Xue M, Do M (2019) Scenario complexity for unmanned aircraft system traffic. *AIAA Aviation 2019 Forum*, 3513.
- Zheng N, Geroliminis N (2016) Modeling and optimization of multimodal urban networks with limited parking and dynamic pricing. *Transportation Research Part B: Methodological* 83:36–58.

Zhong R, Huang Y, Chen C, Lam W, Xu D, Sumalee A (2018) Boundary conditions and behavior of the macroscopic fundamental diagram based network traffic dynamics: A control systems perspective. *Transportation Research Part B: Methodological* 111:327–355.

Zhou H, Qin H, Cheng C, Rousseau LM (2023) An exact algorithm for the two-echelon vehicle routing problem with drones. *Transportation Research Part B: Methodological* 168:124–150.